ODAS 2019
19th ONERA-DLR Aerospace Symposium
ONERA DLR

EXPERIMENTAL AND NUMERICAL INVESTIGATIONS OF UNSTEADY BOUNDARY-LAYER TRANSITION ON A DYNAMICALLY PITCHING SUBSCALE HELICOPTER ROTOR BLADE

Armin Weiss* Johannes N. Braukmann Kurt Kaufmann
Institute of Aerodynamics and Flow Technology, German Aerospace Center, DLR (Germany)

Abstract
The presented work tackles the lack of experimental investigations of unsteady boundary–layer transition on rotor blades at cyclic pitch actuation, which are important for accurate performance predictions, for instance for helicopters in forward flight. Unsteady boundary–layer transition positions were measured on the blade suction side of a four–bladed subscale rotor by means of the non–intrusive Differential Infrared Thermography (DIT), which does not require instrumented rotor blades. Experiments were conducted at rotation rates corresponding to Mach and Reynolds numbers at 75 % rotor radius of $\mathrm{M}_{75} = 0.11, 0.22$ and $\mathrm{Re}_{75}/10^5 = 1.7, 3.5$ and at varying cyclic blade pitch settings. The setup allowed to sample boundary–layer transition across the outer 55 % of the rotor radius. The study is complemented by numerical simulations including boundary–layer transition modelling based on semi–empirical transition criteria. For the first time, the work successfully applies DIT to capture unsteady boundary–layer transition on the blade suction side on rotating blades. Promising results reveal a plausible development of detected boundary–layer transition positions over the pitch cycle, a reasonable comparison to experimental results obtained using the established σc_p method and noticeable agreement to numerical simulations.

NOMENCLATURE

c	Chord length, $c = 0.072\,\mathrm{m}$
f_{rotor}	Rotation frequency of rotor, Hz
f_{mirror}	Rotation frequency of rotating mirror, Hz
$I_{\mathrm{pos\ 1\|2}}$	Image gray levels at pos 1 or pos 2, counts
ΔI_{DIT}	DIT signal, counts
k	Turbulent kinetic energy, $\mathrm{m}^2/\mathrm{s}^2$
k_{75}	Reduced frequency, $k_{75} = c/(2 \cdot 0.75\,R)$
N	Number of acquired images at pos 1|2
pos 1|2	Azimuth positions at image acquisition
r	Coordinate in radial direction, m
R	Rotor radius, $R = 0.650\,\mathrm{m}$
t	Time, s
t/T	Phase of pitch cycle, $t/T = t f_{\mathrm{rotor}}$
Tu	Turbulence intensity
U_{loc}	Local flow velocity, m/s
x	Coordinate in chordwise direction, m
v_∞	Wind tunnel flow velocity, m/s
β	Angle between rotor axis and axis of rotating mirror, deg
Θ_{75}	Blade pitch angle at $r/R = 0.75$, deg
$\bar{\Theta}_{75}$	Collective pitch angle at $r/R = 0.75$, deg
$\hat{\Theta}$	Amplitude of cyclic pitch setting, deg
$\uparrow$	Upstroke, increasing pitch angle
$\downarrow$	Downstroke, decreasing pitch angle

AHD	Boundary–layer transition criterion according to Arnal, Habiballah and Delcourt
CFD	Computational Fluid Dynamics
DIT	Differential Infrared Thermography
DLR	German Aerospace Center
NASA	National Aeronautics and Space Administration
ONERA	French aeronautics, space and defense research lab
RTG	Rotor Test facility of the DLR in Göttingen
RBT	Rotor Blades Transition
TAU	Unstructured finite-volume CFD code
TS	Tollmien–Schlichting
URANS	Unsteady Reynolds–averaged Navier-Stokes
SLS	Strained–Layer Supperlattice

*corresponding author, email: armin.weiss@dlr.de

1. INTRODUCTION

Laminar–turbulent boundary–layer transition strongly affects the power requirement of helicopter rotors. Numerical simulations of rotor aerodynamics often do not consider boundary–layer transition. This is due to a lack of appropriate transition models, which must account for the complex three–dimensional and unsteady flow conditions of a rotor in forward flight, and which need experimental data for validation.

Measurements of unsteady boundary–layer transition on rotor blades for the validation of transition models are still a challenging task. Many experiments reduce the complexity of a rotor setup by

investigating boundary–layer transition on periodically pitching airfoils equipped with locally installed fast–response hot–film sensors[1] or dynamic pressure transducers[2]. The application of these techniques in the rotating frame demands laborious effort for sensor integration into the model and yields results at discrete locations only. This was demonstrated in experiments using hot–film sensors integrated into the blades of a sub–scale helicopter model[3] or pressure transducers in dynamically pitching Mach–scaled rotor blades[4].

Infrared imaging is well–established for boundary–layer transition detection in steady aerodynamics, such as for rotors in hover[5] or climb[6] conditions. Differential Infrared Thermography (DIT) is a non–intrusive optical alternative to local, blade–mounted sensors for the detection of unsteady boundary–layer transition. The basic idea is to subtract two infrared images taken with a short time delay in order to detect the intermediate transition motion. The principle was demonstrated in proof–of–concept experiments[7], validated against hot-films and dynamic pressure sensors[8] and optimized for various experimental conditions[9].

Recently, Overmeyer et al.[10] applied DIT to the pressure side of a large–scale model rotor in forward flight conditions showing promising results. Nevertheless, some questions regarding the interpretation of results remained unanswered, most probably due to the influence of the azimuthally varying stagnation temperature of the flow. Gardner et al.[11] investigated boundary–layer transition on the rotor blade suction side of a full–scale EC135 helicopter in forward flight by means of DIT. Due to the challenging experimental setup, e.g. the varying and large distance between the observation helicopter and the test object during formation flight, only a few data points were presented, where boundary–layer transition was indicated. To the authors knowledge, a systematic experimental study of unsteady boundary–layer transition on a helicopter rotor at cyclic pitch is still missing.

Current approaches to boundary-layer-transition modeling for Computational Fluid Dynamics (CFD) codes face difficult challenges when implemented into rotating systems. Recent activities focused on boundary–layer transition computations of the NASA 'PSP–rotor' experiment[5] in hover[12,13,14,15] and of the S–76 rotor[16]. The results varied in their performance prediction due to a disparity regarding the prediction of transition positions, which prove the sensitivity and relevance of the topic.

Investigations at DLR and ONERA have shown that approximate transition modeling in unsteady Reynolds–averaged Navier-Stokes (URANS) simulations can provide an improved prediction of the rotor performance in hover[17,18] and forward flight[18,19] while using relatively coarse grids, which are more applicable to industrial aircraft development efforts. The GOAHEAD data set[3] was used for validation, but the available hot-film data is too sparsely sampled to provide reliable validation of the codes.

In the framework of a DLR–ONERA cooperation, boundary–layer–transition computations[20] were performed and showed promising results using experimental data sets obtained on a two–bladed Mach–scaled rotor at collective[6] and cyclic[4] pitch conditions in the Rotor Test Facility at DLR Göttingen (RTG). Still, the computations on the cyclic test case showed the need for spatially highly resolved measurements of unsteady boundary–layer transition.

The scope of this paper is to investigate unsteady boundary–layer transition on the four–bladed subscale model rotor on the well–instrumented rotor test stand RTG[4]. The experiments include a variation of the cyclic blade pitch angles at different rotation frequencies. The main objectives are to evaluate the feasibility of DIT in rotor conditions in terms of transition signal strength of a state–of–the–art infrared camera using a strained–layer superlattice (SLS) detector and to adapt the evaluation routines to rotor conditions. Measured data are further compared to unsteady boundary–layer transition computations using the DLR-TAU code and the Rotor Blades Transition (RBT) tool as recently applied by Kaufmann et al.[20]. The result is the first systematic study of unsteady boundary–layer transition on a rotor suction side by means of DIT on rotating blades including a comparison to numerical prediction capabilities at DLR.

2. EXPERIMENTAL AND NUMERICAL SETUP

2.1. Experimental Setup

The experiments were conducted in the rotor test facility (RTG) of the German Aerospace Center (DLR) in Göttingen[4]. The four–bladed rotor (see Fig. 1) was placed in the test section of an Eiffel–type wind tunnel with a nozzle cross section of $1.6\,\mathrm{m}$ x $3.4\,\mathrm{m}$. The rotor axis is horizontal to prevent ground effects. An axial inflow of $v_\infty = 2.2\,\mathrm{m/s}$ was provided to prevent recirculation of tip vortices and blade–vortex interaction.

The rotor blades (see Fig.2) were made out of carbon fiber reinforced plastic, had a radius of $R = 0.650\,\mathrm{m}$, a chord length of $c = 0.072\,\mathrm{m}$ and a relative thickness of $9\,\%$. The blades were equipped with the DSA–9A helicopter airfoil and comprised a parabolic SPP8 tip without anhedral[21], which

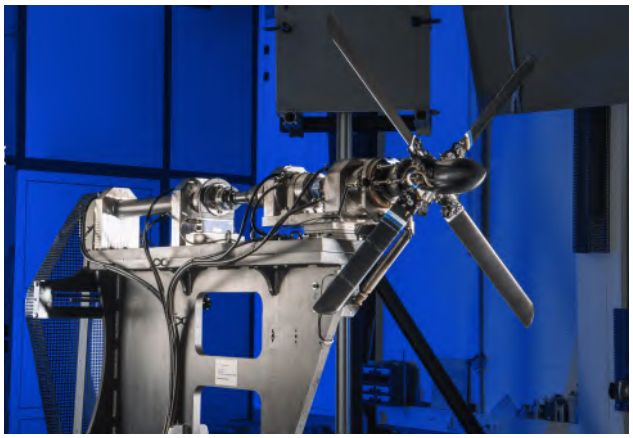

Figure 1: Rotor equipped with four *DSA–9A* rotor blades (see Fig. 2) in the RTG at the DLR Göttingen

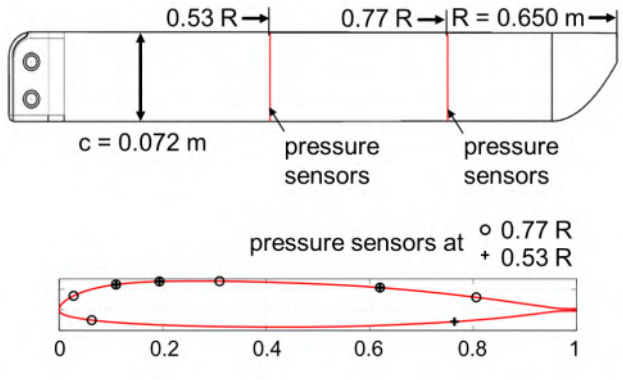

Figure 2: *Top:* Planview of the rotor blade[4] (not to scale) *Bottom:* DSA–9A airfoil and location of pressure sensors

started at 91 % radius and led to a tip chord length of 24 mm (see Schwermer et al.[4] for details). A negative linear twist of $-9.33\,\mathrm{deg}$ was incorporated along the blade's span between $0.25 < r/R < 1$. The investigated blade was equipped with fast response pressure transducers at $r/R = 0.53$ and at $r/R = 0.77$ (see Fig. 2*b*), providing a signal at a bandwidth of 19 kHz.

The rotor head of the RTG featured a swashplate allowing for the adjustment of both collective and cyclic blade pitch angles[4]. The resulting pitch cycle at $r/R = 0.75$ can be described according to Eq. 1.

$$\Theta_{75} = \bar{\Theta}_{75} - \hat{\Theta} \cdot cos(2\pi f_{\mathrm{rotor}} t) \tag{1}$$

In this expression $\bar{\Theta}_{75}$ and $\hat{\Theta}$ are the collective and cyclic pitch settings and $f_{\mathrm{rotor}}t = t/T$ is the relative phase position. In this setting, the pitch cycle started with minimum pitch angle at $t/T = 0$ and reached the maximum at $t/T = 0.5$. While the optical setup was oriented towards a fixed azimuthal blade position, the test rig allowed to scan the entire pitch cycle in the camera's field of view at that azimuthal position[4]. This was realized by slowly rotating the usually stationary lower part of the swashplate, so that the blade pitch cycle swept through the fixed measurement position.

A schematic sketch of the test setup is shown in Fig. 3. Heat lamps were installed above the nozzle outlet in order to increase the temperature difference between laminar and turbulent flow regions on the blade surface. Images were acquired with a FLIR Systems™X8500sc SLS high speed infrared camera. The 14 bit camera had a spectral sensitivity in the long wave infrared range of 7.5 – 12 µm and was mounted with a 50 mm, f/2.5 lens approximately 2 m apart from the investigated blade. The optical setup was completed by a rotating mirror, which was used to capture a stationary image of the moving blade. This enabled longer exposure

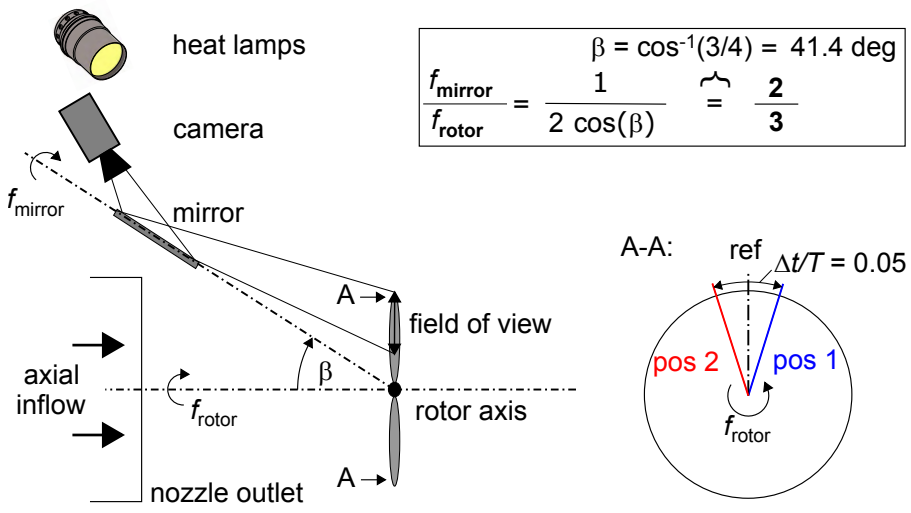

Figure 3: Schematic of rotating mirror setup in off–axis configuration for DIT measurements at the RTG

Table 1: Test conditions

Test case	f_{rotor}, Hz	$\bar{\Theta}_{75}$, deg	$\hat{\Theta}$, deg	Re_{75}	M_{75}	v_∞, m/s	k_{75}
i	11.8	10.1	1.6				
ii	12.0	10.1	2.9	1.7×10^5	0.11	2.2	0.074
iii	11.8	9.9	6.2				
iv	23.6	9.6	6.2	3.5×10^5	0.22	2.2	0.074

times for increased signal strength whilst avoiding motion–blurred images.

An important feature of the rotating mirror is that it allows to capture two successive rotor blade images in the same rotor revolution at different azimuthal positions, which correspond to different pitch phases. The rotating mirror was installed in off–axis configuration as suggested by Raffel and Heineck[22]. It meets the requirement for a ratio of rotation frequencies between rotating mirror and rotor of $f_{\text{mirror}}/f_{\text{rotor}} = 2/3$. The ratio allows image acquisition every third rotor revolution. Consequently, the setup aims to acquire an image pair (at 'pos 1' and 'pos 2', see Fig. 3) at all pitch phases and at a phase difference during a single rotor revolution. This allows to capture the instantaneous boundary–layer transition position associated with the pitch angle at the intermediate phase position (marked as 'ref' in Fig. 3).

The four examined test cases are listed in Tab. 1. The resulting Mach- and Reynolds number as well as the reduced frequency k_{75} are provided at the radius $r = 0.75\,R$. The tested conditions comprise three different pitch amplitudes and two different rotation rates of the rotor, allowing to study the effects of pitch amplitude and frequency independently. Test case ii was selected for comparison to numerical simulations, which are described in the next section.

2.2. Numerical Setup

DLR-TAU[23] is an unstructured finite-volume CFD code solving the compressible Navier-Stokes equations. The temporal discretization of the RBT simulations uses an implicit Euler method with a LUSGS linear solver inside a dual time stepping approach. The turbulence and transition equations are solved by a Roe scheme with a second order state extrapolation and for the diffusive fluxes a second order central scheme is used. The turbulence is modeled using the k-ω SST eddy viscosity model according to Menter[24]. The highly-resolved and partially scale-resolving transition computations on the NASA PSP rotor by e.g. Coder[12] and Vieira et al.[13] have shown the potential of a very detailed transition modeling. Nevertheless, the computational costs of these kind of investigations are still too high for industry–relevant computations. In this study a very coarse grid and an approximate boundary–layer transition method is used, which are interesting for industry–relevant studies due to the low computational costs needed. Approximately 20 000 hours on a central processing unit were needed to converge the cyclic test case ii (see Tab. 1).

The RBT-TAU computations were run on a complete four blade mesh setup-up, which is depicted in Fig. 4. The hybrid mesh consists of a hexahedral grid around the blade and tetrahedral elements in the farfield. The background farfield mesh is integrated with the blade mesh using the chimera technique. A full cylinder of 200 R height and 100 R radius containing the four blades is used for the RBT

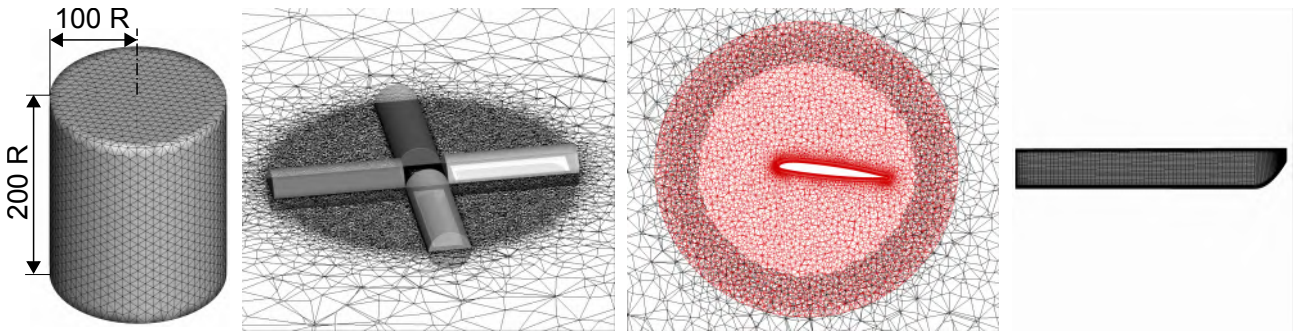

Figure 4: Computational grid domain, chimera setup, grid sections at $r/R = 0.77$ and surface grid (from left to right)

computations, see Fig. 4 (*left*). Each blade mesh of the RBT case comprises 1.5×10^6 points resulting in a total mesh size of 7.7×10^6 nodes. The first wall spacing was set to keep $y^+ < 1$. The blade is discretized with 120 points and 100 points in streamwise and radial direction, respectively. The boundary-layer discretization in wall–normal direction comprises approximately 30 points.

The RBT tool, which is coupled to the DLR-TAU code, will be discussed briefly. For a more detailed description, the reader is referred to Heister et al.[19]. Although the RBT tool is capable of detecting five different types of transition mechanisms, only the criterion to predict Tollmien–Schlichting (TS) transition according to Arnal, Habiballah and Delcourt[25] (AHD) is used in this study. Kaufmann et al.[20] showed in preceding computations of the same rotor in a two–bladed configuration that the transition prediction using all types of transition mechanisms results in an erroneous transition position and the transition prediction is only acceptable, if TS transition is used.

To evaluate the AHD criteron, section cuts at 48 different radii are defined for both the pressure and the suction side. The computed transition onset positions are then used to control the turbulence model. However, the transitional region is not modeled, i.e. point transition is assumed. To compute the local turbulence level Tu , using Eq. 2, the flow velocities U_{loc} and the turbulent kinetic energy k are extracted from the URANS data at a user-defined distance upstream of the corresponding stagnation point.

$$Tu = 1/U_{loc}\sqrt{2/3\,k} \tag{2}$$

To align with the experimental turbulence level, the kinetic energy at the far field boundary has to be set to match the extracted kinetic energy in front of the profile sections. Therefore, the sustaining turbulence concept is locally implemented up to one rotor radius above the rotor in order to reduce the dissipation of the turbulence quantities from the farfield to the rotor[26]. For the DLR-TAU transition criteria computations, an iterative approach was conducted to match the turbulence level of $Tu = 0.09\,\%$ at $r/R = 0.77$. The value for Tu was deduced by Weiss et al.[27], who conducted transition measurements on the two–bladed DSA–9A rotor in the same facility.

3. DATA ACQUISITION AND PROCESSING

Infrared images were acquired every third blade revolution as the blade passed the azimuthal positions pos 1 and pos 2 (see Fig. 3) and at an exposure time of 150 µs. The azimuthal positions were separated in phase by $\Delta t/T = \Delta t f_{\text{rotor}} = 0.05$ at all test conditions. The resulting separation times of the image pairs within the same revolution were $\Delta t = 4.2$ ms and 2.1 ms at $f_{\text{rotor}} = 11.8$ Hz and 23.6 Hz, respectively. The separation time was limited by the camera's pixel clock and the selected region of interest, which covers 55 % of the rotor radius at a resolution of ≈ 2 px/mm (see Fig. 5). At each test condition, the full pitch cycle is covered by acquisition of two times ≈ 1000 images (at pos 1 and pos 2), respectively. The resulting phase resolution of the DIT signal is $\Delta t/T \approx 0.001$. Since image pairs are acquired every third blade revolution, data acquisition took approximately 4 min and 2 min for each data point at $f_{\text{rotor}} = 11.8$ Hz and 23.6 Hz.

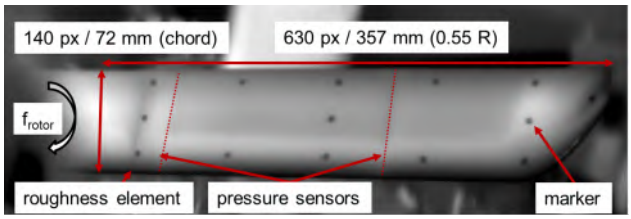

Figure 5: Sample image acquired at f_{rotor} = 12.0 Hz, $\bar{\Theta}_{75} = 10.1$ deg and $\hat{\Theta} = 2.9$ deg

The raw image shown in Fig. 5 was acquired for test case ii. The displayed gray levels on the blade surface scale with temperature and appear darker in regions of comparatively higher heat transfer, for instance close to the leading edge, where the boundary layer is thin, or in the turbulent wake of the roughness element. Other than in measurement campaigns with collective pitch settings only[6], the measured intensity gradients in tangential direction cannot be used for instantaneous boundary–layer transition detection on dynamically pitching rotor blades. Previous studies on 2D pitching airfoils have shown that the spatial gradients in the raw images are biased by the thermal inertia of the model surface[7,9,28]. Hence, the DIT approach is to subtract two infrared images acquired at a small time or phase difference within the pitch cycle to capture the transition motion between the two instants with different pitch angles. With this approach, the time–averaged temperature footprint on the model surface is canceled out. In previous DIT studies the two images were usually acquired in different pitch cycles at a defined phase difference because of the limited temporal resolution of the infrared camera, see e.g. Raffel et al.[7]. Wolf et al.[9] showed that the resulting large time difference between images can cause global temperature drifts in the model surface, which need to be corrected

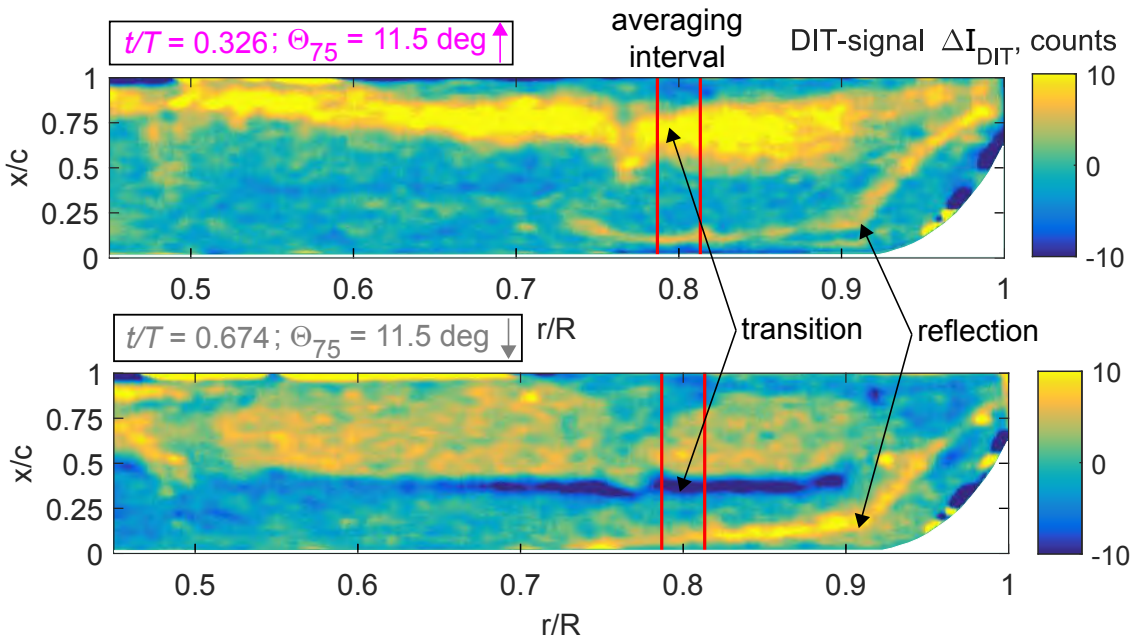

Figure 6: DIT results at f_{rotor} = 12.0 Hz, $\bar{\Theta}_{75} = 10.1\,\text{deg}$ and $\hat{\Theta} = 2.9\,\text{deg}$ at an instantaneous pitch angle of $\Theta_{75} = 11.5\,\text{deg}$ during upstroke ↑ (*top*) and downstroke ↓ (*bottom*)

for. In this study however, the applied infrared camera allowed to capture images during the same rotor revolution at time differences corresponding to acquisition frequencies of up to 476 Hz at the resolution and field of view as described above.

Round markers (see Fig. 5) were applied on the blade to enable image alignment before subtraction of gray levels, associated with the same physical position on the blade, is possible. Marker registration and image alignment were performed with the in–house developed software package *ToPas* (as in Klein et al.[29]). The procedure accounts for rotation and translation within the image plane. Noise was removed by applying a 3×5 moving average filter in chordwise and spanwise directions. The aligned images were sorted by phase and the DIT signal, ΔI_{DIT}, was obtained for each phase according to Eq. 3.

$$\Delta I_{\text{DIT}}\left(t/T\right) = \left[I\left(t/T\right)_{\text{pos1}} - \bar{I}_{\text{pos1}}\right] - \left[I\left(t/T\right)_{\text{pos2}} - \bar{I}_{\text{pos2}}\right] \tag{3}$$

The associated phase t/T corresponds to the mean value of the processed images and the azimuthal position marked as 'ref' in Fig. 3, i.e. $t/T = \left[\left(t/T\right)_{\text{pos1}} + \left(t/T\right)_{\text{pos2}}\right]/2$. Before subtraction of the images at pos 1 and pos 2, tare images (see Eq. 4) are subtracted.

$$\bar{I}_{\text{pos1|2}} = \frac{1}{N}\sum_{i=1}^{N(\approx 1000)}\left[I\left(t/T\right)_{\text{pos1|2}}\right]_i \tag{4}$$

Subtraction of these images accounts for any systematic differences between the two azimuthal positions, for instance due to inhomogeneous heating of the rotor disc area. After image subtraction the obtained DIT signal was dewarped to blade coordinates in Matlab applying a projective image transformation function to detected and physically measured marker coordinates.

4. RESULTS

Selected DIT results obtained at f_{rotor} = 11.8 Hz, $\bar{\Theta}_{75} = 10.1\,\text{deg}$ and $\hat{\Theta} = 2.9\,\text{deg}$ during upstroke (↑) and downstroke (↓) are shown in Fig. 6 *(top)* and Fig. 6 *(bottom)*. The results were obtained at the same instantaneous pitch angle of $\Theta_{75} = 11.5\,\text{deg}$. The pitch cycle and the pitch angles of associated image pairs are plotted against phase in Fig. 7 *(top)*. During upstroke at increasing pitch, boundary–layer transition moves upstream between the first and second image. Hence, the spatial extent of more efficiently cooled blade surface is increased and the DIT signal is expected to be positive. The opposite holds during downstroke. This is confirmed by the results in Fig. 6. At $t/T = 0.326$ the DIT signal is positive and appears as yellow band between $0.5 < r/R < 0.9$. The band indicates the three–dimensional distribution of boundary–layer transition across the blade span. At inboard radii, transition occurs more downstream as compared to further outboard. The result at $t/T = 0.674$ on the other hand reveals a prominent band of nega-

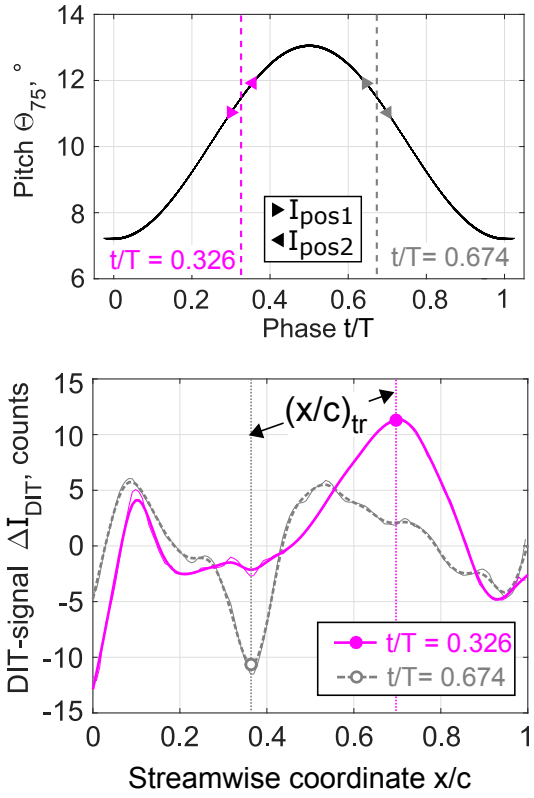

Figure 7: *Top:* Phase positions of images corresponding to results displayed in Fig. 6 *Bottom:* Spanwise averaged DIT signal at $r/R = 0.8$ with detected transition positions marked with circles for test case presented in Fig. 6

tive values for ΔI_{DIT} between $0.65 < r/R < 0.9$, which are caused by the downstream movement of boundary–layer transition during downstroke. Both results in Fig. 6 exhibit an arc–shaped (yellow) band of positive values for ΔI_{DIT} along the leading edge at $r/R > 0.75$ with a kink at $r/R \approx 0.92$. The structure is due to reflections, which hamper the DIT signal in the respective region. Closer examination of Fig. 6 *(top)* reveals wedge–shaped structures in the DIT signal at $r/R = 0.49$ and at $r/R = 0.77$. The structures are due to premature boundary–layer transition induced by the roughness element and the pressure tap cavities at the respective radial positions.

The transition position is quantified at $r/R = 0.8$ by analysis of the spanwise averaged signal confined by the red lines in Fig. 6 (*top*) and Fig. 6 (*bottom*). The averaging interval corresponds to $\Delta r = 10\,\mathrm{mm}$ and the corresponding mean signals are plotted versus the streamwise coordinate x/c in Fig. 7 (*bottom*). According to Richter et al.[8] and Gardner et al.[28], the circled signal peaks in the graph correspond to the transition positions $(x/c)_{\mathrm{tr}}$, which are equivalent to the positions corresponding to 50 % turbulent intermittency or to the peak RMS signal of fast response pressure transducers. A comparison of the peak positions reveals that the corresponding boundary–layer transition position is $\Delta(x/c)_{\mathrm{tr}} \approx 0.3$ further upstream at $t/T = 0.674$ during downstroke as compared to $t/T = 0.326$ during upstroke. Considering that the associated pitch angle is the same for both phases, the observed difference is due to both aerodynamic and temperature–lag related hysteresis effects as previously examined by Gardner et al.[28] and Wolf et al.[9] and further discussed below.

4.1. Effect of pitch rate

The effect of pitch rate is studied by examining the DIT–signal strength and the transition movement over the pitch cycle and comparing DIT results to data obtained using the σc_{p} method. According to the definition of the pitch cycle in Eq. 1 the corresponding pitch rate yields

$$\frac{d\Theta}{dt} = 2\pi f_{\mathrm{rotor}} \hat{\Theta} \cdot sin(2\pi f_{\mathrm{rotor}} t). \tag{5}$$

In this study, the pitch rate was altered by an independent variation of the pitch amplitude $\hat{\Theta}$ and the rotation frequency f_{rotor}.

4.1.1. Variation of pitch amplitude

The pitch amplitude was varied between $\hat{\Theta} = 1.6, 2.9$ and $6.2\,\mathrm{deg}$ at a collective pitch angle of $\bar{\Theta}_{75} = 10.0 \pm 0.1\,\mathrm{deg}$ according to the conditions for test cases i,ii and iii in Tab. 1.

For the three test cases, the DIT signal at $r/R = 0.74$ was analyzed at all sampled pitch phases. An automated algorithm detected the peak height of ΔI_{DIT} and the corresponding transition position $(x/c)_{\mathrm{tr}}$ as described above. Peaks were only accepted above a threshold value of $|\Delta I_{\mathrm{DIT}}| > 5$ and obvious invalid outliers were removed, for instance in phase ranges close to the pitch minimum or at streamwise positions in the vicinity of the leading and trailing edges. Detected peak values and corresponding boundary–layer transition positions are plotted against phase in Fig. 8.

As observed by Wolf et al.[9], the DIT peaks in Fig. 8 (*top*) are large when the transition motion between the images at pos 1 and pos 2 is fast. Therefore, the peak values have a sinusoidally–shaped distribution over the pitch cycle t/T. The data exhibit significant scatter due to the limited signal to noise ratio of the DIT signal, which is in line with the generally small absolute peak strength of less than 25 counts overall. The signal strength increases

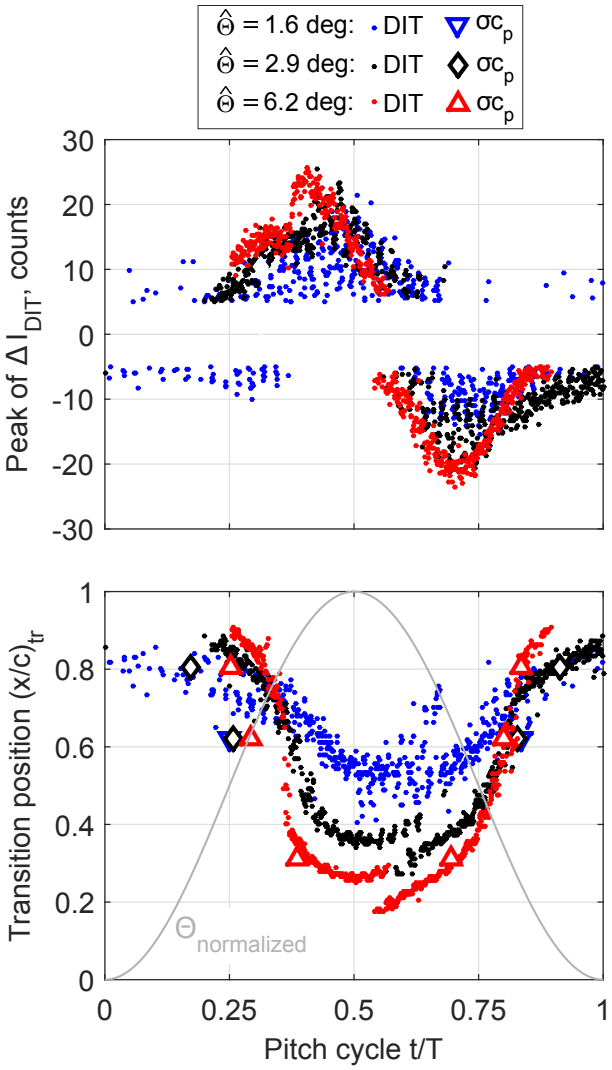

Figure 8: Pitch amplitude effect on DIT signal peak (*top*) and boundary-layer transition (*bottom*) versus pitch cycle for test cases i, ii and iii (see Tab. 1); DIT data extracted at $r/R = 0.74$, σc_p data at $r/R = 0.77$

and the scatter decreases with increasing pitch amplitude, which consequently favors the detectability of boundary–layer transition by means of DIT. The increased peak to noise ratio at higher pitch amplitudes is due to the larger displacement of the boundary–layer transition position between the two images, which are acquired at the same phase differences $\Delta t/T$ for all cases. The larger transition displacement in turn leads to an increased peak in the difference signal of the respective temperature distributions. This was demonstrated by Wolf et al.[9] who applied the DIT method to static infrared transition data, which was obtained at different angles of attack on a two–dimensional DSA–9A airfoil (see Fig. 8 in Ref.[9]). However, Wolf et al.[9] also showed that if the boundary–layer displacement between the two images is too large, for instance due to an excessive phase separation $\Delta t/T$ between images, the detectability is debased due to the existence of a double peak in the signal.

The transition positions associated with the DIT peaks are plotted versus the pitch cycle in the lower graph of Fig. 8. The qualitative evolution of the pitch angle is added to the graph in gray to ease interpretation of the results. The DIT data is extracted at $r/R = 0.74$, which is in the vicinity of the pressure transducers at $r/R = 0.77$ but outside the turbulent wedge emanating from the sensor cavities. As expected, transition moves upstream during upstroke at increasing pitch angles and downstream during downstroke at decreasing pitch angles for all test cases. The increased scatter at lower pitch amplitudes is also reflected in the detected transition positions reaching from $\Delta\,(x/c)_{\mathrm{tr}} \approx 0.15$ at $\hat{\Theta} = 1.6\,\mathrm{deg}$ to $\Delta\,(x/c)_{\mathrm{tr}} \approx 0.05$ at $\hat{\Theta} = 6.2\,\mathrm{deg}$ if the systematic error close to the pitch maximum is neglected. Transition detection is difficult at the reverse points of the pitch cycle because DIT relies on changes of the boundary–layer transition position. Similar to the findings in previous DIT studies[7,8,9] the data gap at the downstream transition reverse point close to the pitch minimum is larger than the phase range with spurious data at the reverse point close to pitch maximum. The increased gap at the downstream reverse point is due to a lower peak–to–noise ratio towards the trailing edge as a result of an increasing transition length at smaller adverse pressure gradients. At the upstream reversal of $(x/c)_{\mathrm{tr}}$, the detected peak positions switch back and forth between distinct chordwise positions, and the detected transition motion does not follow a steady curvature. Richter et al.[8] and Wolf et al.[9] found that this behavior originates from the coexistence of the positive and negative signal peaks, associated with the upstream and downstream movement of transition (see Fig. 7, *bottom*).

A comparison of the transition movement between the three pitch amplitudes in the bottom graph of Fig. 8 shows that the streamwise range, where boundary–layer transition occurs is extended to further upstream and downstream positions as the pitch amplitude is increased, which leads to an intersection of the scatter plots at $t/T \approx 0.35$ and $t/T \approx 0.81$. The phases at intersection are in the vicinity to the phases corresponding to the respective mean pitch angle, i.e $t/T = 0.25$ and $t/T = 0.75$. The same effect was observed by Richter et al.[30] who studied the pitch amplitude effect on unsteady boundary–layer transition on a two–dimensional (2D) EDI-M109 airfoil. They showed that the intersection points correspond to

the phases, where the section lift coefficient is comparable.

For comparison to DIT results, the σc_p method[2] was applied. The detected phases corresponding to boundary–layer transition at the respective sensor positions are marked by symbols in Fig. 8. The σc_p results compare well during downstroke and comprise a maximum difference of $\Delta\,(x/c)_{\mathrm{tr}} \approx 0.25$ during upstroke. The upstream shift compared to the DIT results at $t/T < 0.5$ can be attributed to premature boundary–layer transition at the pressure tap cavities as observed in Fig. 6 (*top*) at $r/R = 0.77$.

The measured transition movement exhibits a phase lag with respect to the blade pitch motion (see Eq. 6) for both DIT and σc_{p} data.

$$\Delta\,(t/T)_{\mathrm{tr}} = \frac{(t/T)_{\mathrm{tr},\uparrow} + (t/T)_{\mathrm{tr},\downarrow}}{2} - 0.5 \tag{6}$$

For the data presented in Fig. 8 (*bottom*) the phase lag measured by the median DIT signals at $(x/c)_{\mathrm{tr}} = 0.62$ ranges between $0.08 < \Delta\,(t/T)_{\mathrm{tr}} < 0.09$, which is significantly larger than $0.04 < \Delta\,(t/T)_{\mathrm{tr}} < 0.05$ as measured by means of σc_{p}. A phase lag was also observed by Richter et al.[31], who investigated unsteady boundary–layer transition on a pitching DSA–9A airfoil using hot–films. They showed that for a given cyclic pitch setting the phase lag increases linearly with the chordwise coordinate. This leads to an asymmetric transition movement between upstroke and downstroke, which can also be distinguished for the two higher pitch amplitudes in Fig. 8 (*bottom*). In contrast to their study, the lag observed for the DIT data in Fig. 8 is due to both aerodynamic and temperature-lag related measurement hysteresis, which is elaborated further below.

4.1.2. Variation of pitch frequency

The effect of pitch frequency is investigated by changing the rotation rate of the rotor from $f_{\mathrm{rotor}} = 11.8\,\mathrm{Hz}$ to $f_{\mathrm{rotor}} = 23.6\,\mathrm{Hz}$ at conditions corresponding to test cases iii and iv in Tab. 1. The corresponding DIT peaks and the measured transition positions are displayed in the upper and lower graphs in Fig. 9. The qualitative evolution of both DIT–signal peaks and transition positions over the pitch cycle is similar to the results discussed in Fig. 8. The top of Fig. 9 reveals that the DIT signal decreases as f_{rotor} is increased. For all cases, the phase separation between an image pair considered for a DIT data point was chosen according to $\Delta t f_{\mathrm{rotor}} = 0.05$. Therefore, the time difference between two images is halved as the frequency is doubled. Hence, at $f_{\mathrm{rotor}} = 11.8\,\mathrm{Hz}$ the model surface has twice the time to react to the different surface temperature as a result of the boundary–layer transition displacement between acquisition of the two associated images. The change of the boundary–layer transition position is the same for both cases as it depends on the difference in pitch angle $\Delta\Theta = (d\Theta/dt) \cdot \Delta t$. Because the phase separation $\Delta t f_{\mathrm{rotor}}$ between images is not changed for the compared cases the difference in pitch angle is also the same, i.e. $\Delta\Theta = 2\pi\Delta t f_{\mathrm{rotor}} \cdot sin(2\pi f_{\mathrm{rotor}} t)$ with Eq. 5.

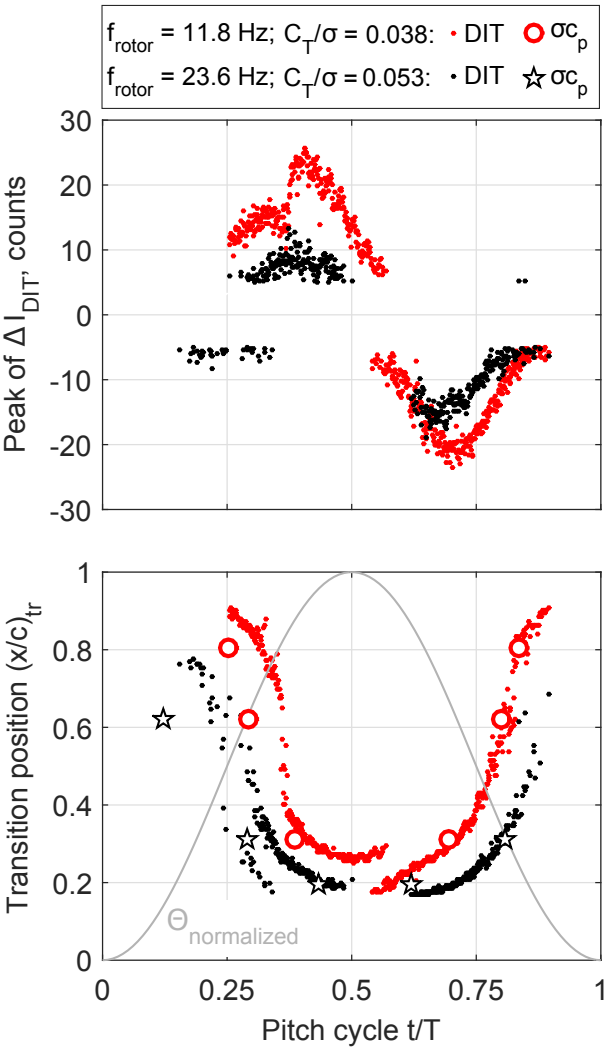

Figure 9: Pitch frequency effect on DIT signal peak and boundary-layer transition versus pitch cycle for test cases iii and iv (see Tab. 1); DIT data extracted at $r/R = 0.79$, σc_p data at $r/R = 0.77$

In Fig. 9 (*top*), a kink in the sinusoidally shaped evolution of the DIT peaks can be distinguished at $t/T \approx 0.32$, which is associated with sparse transition data in the graph below. This kink is due to

the high rate of the transition movement at that phase position, which can be seen in the bottom graph. As previously mentioned by Richter et al.[8] and shown by Wolf et al.[9], the DIT signal peak levels out as the transition movement is too large between the acquisition of the corresponding infrared images. This artifact could be principally tackled by reducing the image separation time, which in this case was adopted to the case at $f_{\text{rotor}} = 23.6$ Hz in order to keep the delta in phase constant between two images.

The measured boundary–layer transition positions at $f_{\text{rotor}} = 23.6$ Hz in Fig. 9 (*bottom*) exhibit larger scatter than at $f_{\text{rotor}} = 11.8$ Hz. Especially between $0.25 < t/T < 0.35$, some spurious values for $(x/c)_{\text{tr}}$ exist, which are consistently too far upstream for $\approx 15\,\%$ of the chord. In general, the unsteady transition results are consistently further upstream at $f_{\text{rotor}} = 23.6$ Hz. Since the axial inflow remains unchanged between both cases, the inflow angle to the rotor blades increases at higher rotation rates. The resulting larger effective angle of attack causes a higher blade loading of $C_T/\sigma = 0.053$ at $f_{\text{rotor}} = 23.6$ Hz as compared to $C_T/\sigma = 0.038$ at $f_{\text{rotor}} = 11.8$ Hz, which in turn results in boundary–layer transition positions further upstream. The higher Reynolds number at $f_{\text{rotor}} = 23.6$ Hz also results in boundary–layer transition further upstream. Hence, the results in the lower graph in Fig. 9 include the superposed effects of Reynolds number and blade loading.

As for the cases presented in Fig. 8, the σc_p results indicate boundary–layer transition further upstream during upstroke and good agreement to DIT results during downstroke. At $(x/c)_{\text{tr}} = 0.62$ in Fig. 9 (*bottom*), only a single peak in the σc_p measuring signal could be identified which was attributed to the upstroke motion. At $(x/c)_{\text{tr}} = 0.31$, the phase lag between the pitch motion and the transition movement (see Eq. 6), as measured by the pressure transducers, increases from $\Delta(t/T)_{\text{tr}} = 0.04$ to $\Delta(t/T)_{\text{tr}} = 0.05$ as the pitch frequency is increased. The equivalent phase lag measured with DIT is consistently higher and increases from $\Delta(t/T)_{\text{tr}} = 0.06$ to $\Delta(t/T)_{\text{tr}} = 0.07$ at increasing f_{rotor}. As mentioned above, the increased delay for DIT results can be attributed to additional thermal hysteresis. Despite this, the σc_p results are in line with the findings of Richter et al.[31] on the 2D pitching DSA–9A airfoil. At $M = 0.30$ and $Re = 1.8 \times 10^6$, they measured phase lags between $0.005 < (t/T)_{\text{tr}} < 0.028$, with greater lags at larger frequencies and at a maximum pitch rate of $d\Theta/dt = 290\,\text{deg}/\text{s}$. The higher level of $\Delta(t/T)_{\text{tr}}$ in this study can be attributed to the higher maximum pitch rates, which are $d\Theta/dt = 452\,\text{deg}/\text{s}$ at $f_{\text{rotor}} = 11.8$ Hz and $d\Theta/dt = 904\,\text{deg}/\text{s}$ at $f_{\text{rotor}} = 23.6$ Hz.

4.1.3. Pitch rate effect on hysteresis

The effects of pitch amplitude and frequency on the transition hysteresis become more clear in the upper and lower graphs in Fig. 10, where the measured transition positions are plotted as function of the instantaneous pitch angle for the test cases presented in Fig. 8 and Fig. 9, respectively. For reasons of clarity, the data in this figure has been reduced. All data samples were binned to 50 windows throughout the cycle and each bin was median filtered to smooth out existing scatter. The bars confine the minimum and maximum of the data considered for each bin, respectively.

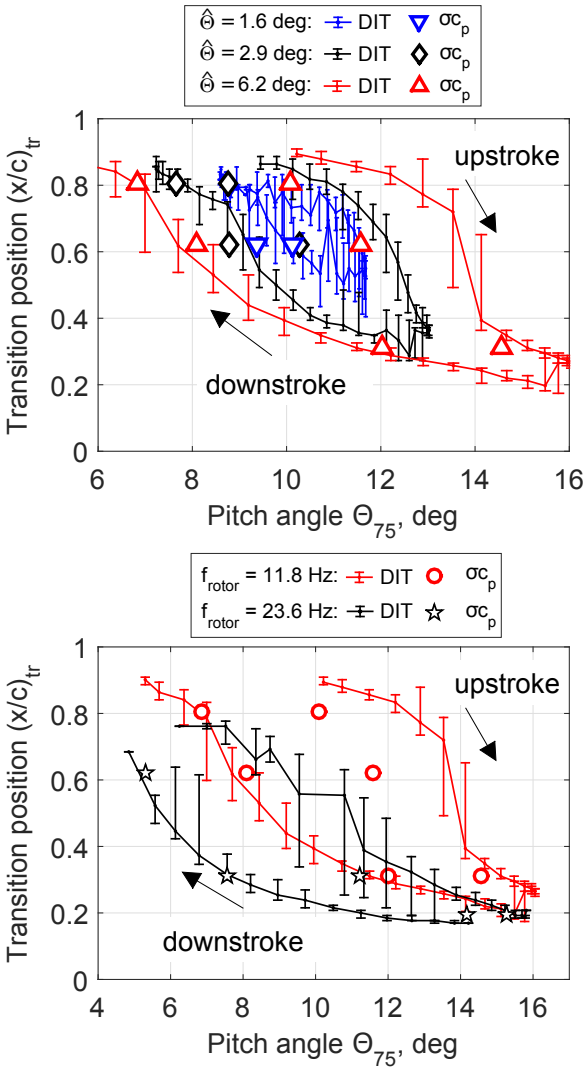

Figure 10: Unsteady boundary–layer transition versus pitch angle for different pitch amplitudes, i.e. test cases i, ii and iii, see Tab. 1 (*top*), and for different pitch frequencies, i.e. test cases iii and iv (*bottom*)

The results in the upper graph of Fig. 10 indicate that the hysteresis, i.e. the difference in pitch angle at equal transition position, increases with pitch amplitude. The finding confirms the results in the pitch amplitude study of Richter et al.[30] and extends the applicability to rotor conditions. The asymmetry of the branches between upstroke and downstroke due to hysteresis effects, especially at $\hat{\Theta} = 6.2\,\mathrm{deg}$, is more pronounced by the representation in Fig. 10 than in Fig. 8, which displays the same transition positions against pitch cycle. Moreover, a smaller hysteresis is measured by σc_p as compared to using DIT. This holds as well for the transition positions of the test cases used to study the effect of pitch frequency in the lower graph of Fig. 10, i.e. the hysteresis measured with DIT exceeds the values obtained using σc_p.

In this work, the effect of increased pitch frequency cannot be studied independently as the blade loading and Reynolds number are increased at higher rotating speeds, as well. This is reflected by the upstream shift of $(x/c)_{\mathrm{tr}}$ at $f_{\mathrm{rotor}} = 23.6\,\mathrm{Hz}$ as compared to $f_{\mathrm{rotor}} = 11.8\,\mathrm{Hz}$ in Fig. 10 (*bottom*). Richter et al.[31] measured the isolated effect of pitch frequency on the transition hysteresis using hot–films on a pitching 2D DSA–9A airfoil at $\bar{\Theta} = 5\,\mathrm{deg}, \hat{\Theta} = 7\,\mathrm{deg}, M = 0.30$ and $Re = 1.8 \times 10^6$. When changing the pitch frequency on a 2D airfoil at constant inflow, the angle of incidence is not altered in the same manner as for the rotor conditions in this study. The 2D results[31] indicate a larger hysteresis $\Delta\Theta$ at higher pitch frequencies when compared at the same $(x/c)_{\mathrm{tr}}$.

Wolf et al.[9] studied the effect of both pitch amplitude and frequency on the transition hysteresis using the same 2D DSA–9A airfoil model as Richter et al.[8] and showed that the hysteresis obtained by σc_p and DIT scales with the respective pitch rate (see Eq. 5). The hystereses measured in these two studies[8,9] are plotted as a function of pitch rate in Fig. 11 (*top*) for DIT with filled symbols and for σc_p with open symbols.

The pitch rate associated to each data point is calculated as the mean value between the two phases when transition passes the chordwise position of the respective pressure transducers. Richter et al.[8] extracted the data at $(x/c)_{\mathrm{tr}} = 0.22$ and at $(x/c)_{\mathrm{tr}} = 0.23$ for DIT and σc_p, respectively, whereas the data from Wolf et al.[9] is acquired at $(x/c)_{\mathrm{tr}} = 0.31$. The graph is complemented by the hystereses measured in this study at $(x/c)_{\mathrm{tr}} = 0.62$ and at $(x/c)_{\mathrm{tr}} = 0.31$. At these chordwise positions, data for both DIT and σc_p could be extracted for the test cases used to study the effect of pitch amplitude (in blue) and pitch frequency (in orange). The observed trends in literature[8,9], i.e. the increasing

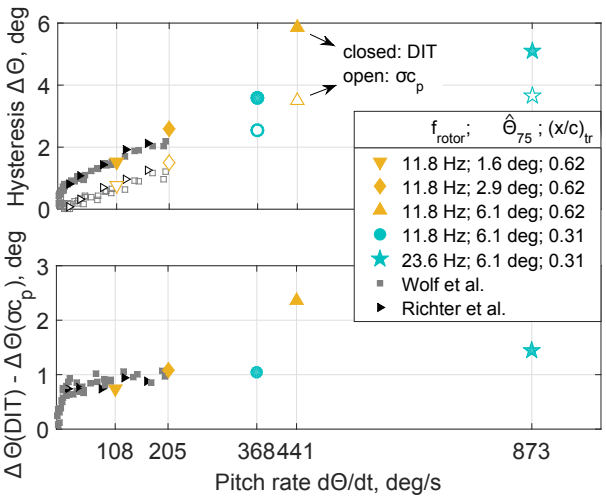

Figure 11: Hysteresis obtained with DIT and σc_p (*top*) and temperature–lag related hysteresis (*bottom*) as function of pitch rate with comparison to results from Wolf et al.[9] and Richter et al.[8]

hysteresis at increasing pitch rates for results obtained by both DIT and σc_p are confirmed by the data presented here. Additionally, the results from this work extend the range of existing data from pitch rates of $d\Theta/dt < 200\,\mathrm{deg/s}$ to pitch rates up to $d\Theta/dt = 873\,\mathrm{deg/s}$, while providing the first transition hysteresis data set obtained on rotating blades so far.

The hysteresis obtained with DIT additionally includes a temperature–lag related hysteresis due to the model surface time response to the changing temperature footprint as result of the boundary–layer transition displacement[8,9,28]. Assuming that the hysteresis values obtained by σc_p display the aerodynamic hysteresis only, the differences between the results from DIT and σc_p, $\Delta\Theta(DIT) - \Delta\Theta(\sigma c_p)$, express the temperature–lag related measurement hysteresis of DIT[9]. The measurement hysteresis is plotted at the bottom of Fig. 11 as a function of pitch rate and the findings of Wolf et al.[9] indicate a convergence of $\Delta\Theta(DIT) - \Delta\Theta(\sigma c_p)$ to $\approx 1\,\mathrm{deg}$, which includes the results from Richter et al.[8]. The prescribed trend is confirmed by all data points from the present study, except for the outlier at $d\Theta/dt = 441\,\mathrm{deg/s}$. Wolf et al.[9] showed that the measurement hysteresis is minimized by limiting the phase separation between the images acquired for DIT to $\Delta t f < 0.01$, which applies for their data in Fig. 11. The results in this study are acquired at phase differences of $\Delta t f_{\mathrm{rotor}} = 0.05$ and the data points from Richter et al.[8] are obtained at phase differences between $0.006 < \Delta t f < 0.046$ with larger values at higher pitch rates. However, the data in the bottom graph of Fig. 11 at $d\Theta/dt < 205\,\mathrm{deg/s}$

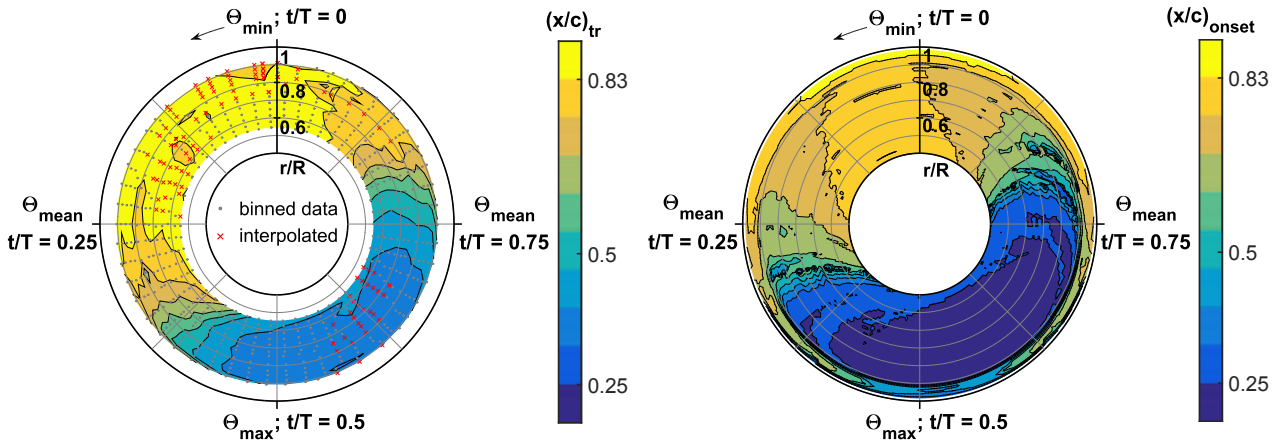

Figure 12: Unsteady boundary–layer transition map at f_{rotor} = 12.0 Hz, $\bar{\Theta}_{75} = 10.1\,\mathrm{deg}$ and $\hat{\Theta} = 2.9\,\mathrm{deg}$ as measured with DIT (*left*) and calculated using the RBT tool in TAU (*right*)

do not indicate any influence of the different phase deltas used.

4.2. Transition map and comparison to numerical results

The test case at f_{rotor} = 12.0 Hz, $\bar{\Theta}_{75} = 10.1\,\mathrm{deg}$ and $\hat{\Theta} = 2.9\,\mathrm{deg}$ was selected for further analysis of transition positions across the blade span over the entire pitch cycle. A comparison between experimental and numerical transition results is provided in Fig. 12. The experimental and numerical 'transition maps' (on the left and right hand side) are displayed using the same contour levels and in polar coordinates, i.e. the pitch cycle with corresponding pitch angles in counter–clockwise direction and the normalized blade radius in radial direction. Overall, the results reveal remarkable qualitative agreement and consistently smaller values obtained in the numerical solution.

The experimental data was analyzed at thirteen radial positions between $0.55 < r/R < 0.94$. For each radius, the detected transition positions were cleared from outliers and valid data was median filtered to 50 bins within the pitch cycle as described above in Sec. 4.1.1. The post processing at $r/R < 0.55$ was hampered due to the turbulent wedges emanating from the roughness element at $r/R = 0.49$ and the pressure transducer cavities at $r/R = 0.53$. At $r/R > 0.94$, transition measurements were biased by residual reflections (see Fig. 6). The resulting contour plot on the left of Fig. 12 is derived from the measured boundary–layer transition positions $(x/c)_{\mathrm{tr}}$ as well as from 2D linearly interpolated data at grid points corresponding to the nearest phase position with available data and the thirteen evaluated radial sections. The phase shift of maximal upstream and downstream transition positions due to hysteresis effects is clearly visible and estimated to be $\Delta(t/T) \approx 0.1$. The data displayed in the bottom left and top right quadrant of the graph at $0.25 < t/T < 0.5$ and $0.75 < t/T < 1$ reveal the gradual upstream and downstream movement of transition during upstroke and downstroke, respectively. The three–dimensional distribution of $(x/c)_{\mathrm{tr}}$ along the blade span can be deduced by the curved isolines between contour levels. At phase instants between $0.3 < t/T < 0.45$ boundary–layer transition occurs further upstream at more outboard radii, whereas between $0.75 < t/T < 0.87$ transition is shifted downstream at higher radii. In the same phase domains, the most outboard data points at $r/R = 0.94$ suggest that boundary–layer transition moves downstream near the blade tip.

For the numerical solution, the AHD criterion estimates the point of primary instability of TS waves. Therefore the RBT tool results on the right hand side of Fig. 12 represent the onset of boundary–layer transition, $(x/c)_{\mathrm{onset}}$, rather than the more downstream location corresponding to 50 % intermittency as detected by DIT and displayed on the left hand side. For this reason, there is a bulk offset between the measured $(x/c)_{\mathrm{tr}}$ and the calculated $(x/c)_{\mathrm{onset}}$. Despite this offset, the two data sets show overall agreement with respect to both hysteresis effects and curvature of contour isolines at $0.25 < t/T < 0.5$ and $0.75 < t/T < 1$. As suggested by the measurement results at the most outboard data points in these phase domains the numerical results underline that boundary–layer transition is shifted downstream close to the blade tip. The behavior can possibly be explained by the influence of the wake vortex system on the local lift distribution across the blade span close to the tip. Tan-

ner and Yaggy[32] measured a discontinuity in the radial distribution of boundary–layer transition using acenaphthene coatings on a hovering NACA0015 rotor at $Re_{tip} = 1.1-1.3\times10^6$. They correlated their finding to the measured discontinuity of the local lift distribution close to the blade tip, possibly due to an interaction of the wall–bounded flow with the wake vortex system. A confirmation of their reasoning for the findings in this study is subject of current investigations. The numerically predicted upstream and downstream motion of boundary–layer transition is faster than the measured data suggests. This is indicated by the closer spacing of contour isolines for the numerical solution as compared to the experimental results at the phases during upstroke and downstroke when Θ_{mean} is passed . Moreover, the numerical results at $r/R > 0.6$ during upstroke and downstroke at $t/T \approx 0.3$ and at $t/T \approx 0.75$ indicate a discontinuous movement of $(x/c)_{onset}$ at $r/R = 0.75$, for instance.

A more detailed comparison between experimental and numerical results is provided in Fig. 13, where the data presented in Fig. 12 are extracted at $r/R = 0.75$ and plotted as function of the pitch cycle.

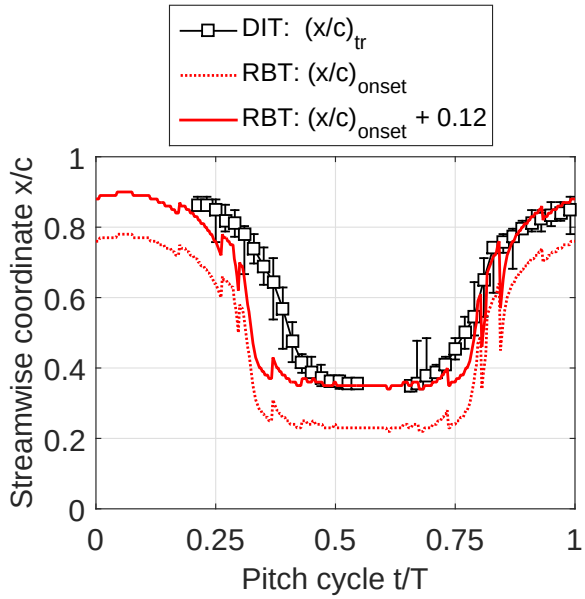

Figure 13: Measured (DIT) and calculated (RBT) transition results at $r/R = 0.75$ for test case ii as presented in Fig. 12

The numerical prediction for $(x/c)_{onset}$ is displayed by the dashed red line and the binned DIT data is represented by squares with bars indicating the scatter of each data bin. The above mentioned discontinuities in $(x/c)_{onset}$ appear as unphysical spikes in the RBT solution, especially at phases when the timerate of change of $(x/c)_{onset}$ is large. The closer spacing of contour level lines observed in Fig. 12 is reflected as larger gradient of the curves for the RBT solution at $t/T = 0.32$ and $t/T = 0.81$. Despite this, there is a noticeable agreement between calculated and measured boundary–layer transition locations, especially during downstroke and when adding a bulk offset of $\Delta(x/c) = 0.12$ to the numerically deduced transition onset positions. With this offset the resulting most upstream and downstream transition positions coincide at $x/c = 0.35$ and at $x/c = 0.89$. Richter et al.[31] measured the intermittent region, i.e. the chordwise difference between fully turbulent flow and transition onset, on a 2D pitching DSA–9A airfoil using hot–films. They found a linear increase of this region from 10 – 20 % of the chord for transition onset positions between $0.2 < (x/c)_{onset} < 0.4$. Taking their findings into account, the offset should be a function of x/c. Despite this, the order of magnitude of $\Delta(x/c) = 0.12$ is justifiable.

5. CONCLUSION

This work presents the first systematic study of measured unsteady boundary–layer transition on the suction side of a subscale helicopter rotor blade equipped with a DSA–9A airfoil. The analysis of measured results was complemented by a comparison to state–of–the–art numerical computations using the semi–empirical AHD criterion to model boundary–layer transition due to Tollmien–Schlichting instabilities. The main findings are summarized as follows:

- Unsteady boundary–layer transition positions were successfully measured. The detectability of transition positions by DIT, in terms of signal peak–to–noise ratio, increases with increasing pitch amplitude and decreases with increasing pitch frequency at constant phase differences between images.
- The independent variation of pitch amplitude and pitch frequency reveal plausible trends with respect to the detected transition movement and the related hysteresis.
- Boundary–layer transition positions detected by the σc_p method show close agreement to DIT results during downstroke and appear consistently more upstream during upstroke. Deviations are due to premature boundary–layer transition triggered at the pressure tap cavities and to the temperature–lag related measurement hysteresis in DIT.

- Hysteresis effects, both aerodynamic and for DIT also temperature–lag related hysteresis, scale with pitch rate. Previous findings obtained on 2D pitching airfoils are confirmed and extended to rotor conditions for pitch rates of up to $d\Theta/dt = 873\,\mathrm{deg}/\mathrm{s}$.

- Transition maps of experimentally and numerically obtained results reveal the three–dimensional distribution of the transition positions along the blade span as function of the pitch cycle. The results obtained by numeric modeling of unsteady boundary–layer transition yield noticeable agreement to experimental results.

ACKNOWLEDGMENTS

The authors thank James T. Heineck (NASA Ames Research center) for the kind loan of the FLIR Systems™X8500sc SLS high speed infrared camera in order to conduct the experiments. The fruitful advise of Christian Wolf, Anthony D. Gardner and Markus Raffel (all DLR Göttingen) as well as the assistance of Markus Krebs (DLR Göttingen) during experiments are also greatfully acknowledged. Moreover, the Gauss Centre for Supercomputing e.V. (www.gauss-centre.eu) is greatfully acknowledged for funding this project by providing computing time on the GCS Supercomputer SuperMUC at the Leibniz Supercomputing Centre (LRZ, www.lrz.de).

REFERENCES

[1] Lorber, P.F., Carta, F.O.: Unsteady Transition measurements on a Pitching Three–Dimensional Wing. In: Fifth Symposium on Numerical and Physical Aspects of Aerodynamic Flows (1992)

[2] Gardner, A.D., Richter, K.: Boundary Layer Transition Determination for Periodic and Static Flows Using Phase-Averaged Pressure Data. Experiments in Fluids **56**(6), 119 (2015). DOI 10.1007/s00348-015-1992-9

[3] Raffel, M., De Gregorio, F., de Groot, K., Schneider, O., Sheng, W., Gibertini, G., Seraudie, A.: On the Generation of a Helicopter Aerodynamic Database. The Aeronautical Journal **115**(1164), 103–112 (2011). DOI 10.1017/S0001924000005492

[4] Schwermer, T., Gardner, A.D., Raffel, M.: A Novel Experiment to Understand the Dynamic Stall Phenomenon in Rotor Axial Flight. Journal of the American Helicopter Society **64**(012004), 1–11 (2019). DOI 10.4050/JAHS.64.012004

[5] Overmeyer, A.D., Martin, P.B.: Measured Boundary Layer Transition and Rotor Hover Performance at Model Scale. In: 55th AIAA Aerospace Sciences Meeting, AIAA 2017-1872. Grapevine, TX, USA (2017). DOI 10.2514/6.2017-1872

[6] Weiss, A., Gardner, A.D., Christian, K., Markus, R.: Boundary-layer transition measurements on mach-scaled helicopter rotor blades in climb. CEAS Aeronautical Journal **8**(4), 613–623 (2017). DOI 10.1007/s13272-017-0263-2

[7] Raffel, M., Merz, C.B.: Differential Infrared Thermography for Unsteady Boundary-Layer Transition Measurments. AIAA Journal **52**(9), 2090–2093 (2014). DOI 10.2514/1.J053235

[8] Richter, K., Wolf, C.C., Gardner, A.D., Merz, C.B.: Detection of Unsteady Boundary Layer Transition Using Three Experimental Methods. In: 54th AIAA Aerospace Sciences Meeting, AIAA 2016-1072, pp. 1–22. San Diego, CA, USA (2016). DOI 10.2514/6.2016-1072

[9] Wolf, C.C., Mertens, C., Gardner, A.D., Dollinger, C., Fischer, A.: Optimization of differential infrared thermography for unsteady boundary layer transition measurement. Experiments in Fluids **60**(19) (2019). DOI 10.1007/s00348-018-2667-0

[10] Overmeyer, A.D., Heineck, J.T., Wolf, C.C.: Unsteady Boundary Layer Transition Measurements on a Rotor in Forward Flight. In: 74th Annual Forum of the American Helicopter Society (2018)

[11] Gardner, A.D., Wolf, C.C., Heineck, J.T., Barnett, M., Raffel, M.: Helicopter rotor boundary layer transition measurement in forward flight using an infrared camera. In: Vertical Flight Society 75th Annual Forum & Technology Display, 75-2019-0037 (2019)

[12] Coder, J.G.: OVERFLOW rotor hover simulations using advanced turbulence and transition modeling. In: 55th AIAA Aerospace Sciences Meeting, AIAA 2017-1432. Grapevine, TX, USA (2017). DOI 10.2514/6.2017-1432

[13] Vieira, B.A.O., Kinzel, M.P., Maughmer, M.D.: CFD hover prediction including boundary-layer transition. In: 55th AIAA Aerospace Sciences Meeting, AIAA 2017-1665. Grapevine, TX, USA (2017). DOI 10.2514/6.2017-1665

[14] Parwani, A., Coder, J.G.: Effect of Laminar–Turbulent Transition Modeling on PSP Rotor Hover Predictions. In: 56th AIAA Aerospace Sciences Meeting, AIAA 2018-0308 (2018). DOI 10.2514/6.2018-0308

[15] Zhao, Q., Wang, J., Sheng, C.: Numerical Simulations and Comparisons of PSP and S–76 Rotors in Hover. In: 56th AIAA Aerospace Sci-

ences Meeting, AIAA 2018-1780 (2018). DOI 10.2514/6.2018-1780
[16] Min, B.Y., Reimann, C.A., Wake, B., Jee, S.K., Baeder, J.D.: Hovering Rotor Simulation using OVERFLOW with Improved Turbulence Model. In: 56th AIAA Aerospace Sciences Meeting, AIAA 2018-1779 (2018). DOI 10.2514/6.2018-1779
[17] Heister, C.: Semi-/empirical transition prediction and application to an isolated rotor in hover. International Journal of Engineering Systems Modelling and Simulation **4**(1-2) (2012). DOI 10.1504/IJESMS.2012.044845
[18] Richez, F., Nazarians, A., Lienard, C.: Assessment of laminar–turbulent transition modeling methods for the prediction of helicopter rotor performance. In: 43rd European Rotorcraft Forum (2017)
[19] Heister, C.C.: A method for approximate prediction of laminar–turbulent transition on helicopter rotors. Journal of the American Helicopter Society **63**(3), 1–14 (2018). DOI 10.4050/JAHS.63.032008
[20] Kaufmann, K., Ströer, P., Richez, F., Lienard, C., Gardarein, P., Krimmelbein, N., Gardner, A.D.: Validation of boundary-layer-transition computations for a rotor with axial inflow. In: Vertical Flight Society 75th Annual Forum & Technology Display, 75-2019-0217 (2019)
[21] Vuillet, A., Allongue, M., Philippe, J.J., Desopper, A.: Performance and Aerodynamic Development of the Super Puma MK II Main Rotor with New SPP 8 blade tip design. In: 15th European Rotorcraft Forum. Amsterdam, Holland (1989)
[22] Raffel, M., Heineck, J.T.: Mirror-Based Image Derotation for Aerodynamic Rotor Measurements. AIAA Journal **52**(6), 1337–1341 (2014). DOI 10.2514/1.J052836
[23] Schwamborn, D., Gerhold, T., Heinrich, R.: The DLR TAU-Code: Recent Applications in Research and Industry. AIAA Journal **32**(8), 2066–2072 (1994). DOI 10.2514/3.12149
[24] Menter, F.R.: Two-equation eddy-viscosity transport turbulence model for engineering applications. AIAA Journal **32**(8), 2066–2072 (1994). DOI 10.2514/3.12149
[25] Arnal, D., Habiballah, M., Coustols, E.: Laminar instability theory and transition criteria in two and three-dimensional flow. La Recherche Aérospatiale (English Edition) **2**, 45–63 (1984)
[26] Spalart, P.R., Rumsey, C.L.: Effective inflow conditions for turbulence models in aerodynamic calculations. AIAA Journal **45**(10), 2544–2553 (2007). DOI 10.2514/1.29373
[27] Weiss, A., Gardner, A.D., Schwermer, T., Klein, C., Raffel, M.: On the effect of rotational forces on rotor blade boundary-layer transition. AIAA Journal **57**(1), 252–266 (2018). DOI 10.2514/1.J057036
[28] Gardner, A.D., Eder, C., Wolf, C.C., Raffel, M.: Analysis of differential infrared thermography for boundary layer transition detection. Experiments in Fluids **58**(9), 122 (2017). DOI 10.1007/s00348-017-2405-z
[29] Klein, C., Engler, R.H., Henne, U., Sachs, W.E.: Application of pressure-sensitive paint for determination of the pressure field and calculation of the forces and moments of models in a wind tunnel. Experiments in Fluids **39**(2), 475–483 (2005). DOI 10.1007/s00348-005-1010-8
[30] Richter, K., Koch, S., Gardner, A.D., Mai, H., Klein, A., Rohardt, C.H.: Experimental Investigation of Unsteady Transition on a Pitching Rotor Blade Airfoil. Journal of the American Helicopter Society **59**(012001), 1–12 (2014). DOI 10.4050/JAHS.59.012001
[31] Richter, K., Koch, S., Goerttler, A., Lütke, B., Wolf, C.C., Benkel, A.: Unsteady Boundary Layer Transition on the DSA-9A Rotor Blade Airfoil. In: 41st European Rotorcraft Forum (2015)
[32] Tanner, W.H., Yaggy, P.F.: Experimental boundary layer study on hovering rotors. Journal of the American Helicopter Society **11**(13), 22–37 (1966). DOI 10.4050/JAHS.11.22